THE JOURNAL OF BIOLOGICAL CHEMISTRY VOL. 282, NO. 7, pp. 5015–5025, February 16, 2007

The C2A-C2B Linker Defines the High Affinity Ca^{2+} Binding Mode of Rabphilin-3A*[S]

Received for publication, July 14, 2006, and in revised form, November 29, 2006 Published, JBC Papers in Press, December 13, 2006, DOI 10.1074/jbc.M606746200

Pierre Montaville[‡1], Christine Schlicker[§1], Andrei Leonov[‡], Markus Zweckstetter[‡2], George M. Sheldrick[§3], and Stefan Becker[‡4]

From the [‡]Department of NMR-based Structural Biology, Max Planck Institute for Biophysical Chemistry, and the [§]Department of Structural Chemistry, University of Göttingen, 37077 Göttingen, Germany

The Ca^{2+} binding properties of C2 domains are essential for the function of their host proteins. We present here the first crystal structures showing an unexpected Ca^{2+} binding mode of the C2B domain of rabphilin-3A in atomic detail. Acidic residues from the linker region between the C2A and C2B domains of rabphilin-3A interact with the Ca^{2+}-binding region of the C2B domain. Because of these interactions, the coordination sphere of the two bound Ca^{2+} ions is almost complete. Mutation of these acidic residues to alanine resulted in a 10-fold decrease in the intrinsic Ca^{2+} binding affinity of the C2B domain. Using NMR spectroscopy, we show that this interaction occurred only in the Ca^{2+}-bound state of the C2B domain. In addition, this Ca^{2+} binding mode was maintained in the C2 domain tandem fragment. In NMR-based liposome binding assays, the linker was not released upon phospholipid binding. Therefore, this unprecedented Ca^{2+} binding mode not only shows how a C2 domain increases its intrinsic Ca^{2+} affinity, but also provides the structural base for an atypical protein-Ca^{2+}-phospholipid binding mode of rabphilin-3A.

Rabphilin-3A belongs to a structurally diverse synaptic protein family whose role is to support and regulate the Ca^{2+}-dependent neurotransmitter release process. A significant number of these proteins share a common structural feature, a tandem of C2 domains. Although specific roles have been attributed to some members of this family, the exact function of rabphilin-3A is still not clear at present. Rabphilin-3A has been shown to interfere with the exocytotic/endocytotic machinery in different secretory systems (1–4). Many studies suggest that rabphilin-3A functions in the synaptic vesicle trafficking processes preceding and/or following the vesicle fusion itself. In PC12 cells, the C2B domain of rabphilin-3A was shown to interact with SNAP25 (synaptosome-associated protein of 25 kDa), regulating the docking step of dense core vesicles (5). Rabphilin knock-out studies carried out in mouse (6) and *Caenorhabditis elegans* (7) have shown that this protein is largely dispensable for the neurotransmitter release process. Nevertheless, in *C. elegans*, rabphilin-3A is able to potentiate the SNARE (soluble *N*-ethylmaleimide-sensitive factor attachment protein receptor) function (7). Very recently, it was shown that, in mouse neurons, rabphilin-3A alters, via its C2B domain, the recovery of synaptic responses after high frequency stimulation (8). With the precise role of rabphilin-3A remaining to be clarified, these most recent findings suggest a fine-tuning function for this protein in the vesicle fusion machinery.

Functionally, two regions of rabphilin-3A have been defined so far: the N-terminal Rab-binding domain, responsible for its interaction with the small GTPases Rab3 and Rab27 (9, 10), and the C-terminal C2 domain tandem fragment, involved in the Ca^{2+}-dependent membrane binding property of the protein (11) as well as in several protein-protein interactions.

The tandem C2 domains of synaptic vesicle proteins function as membrane-targeting modules, activated upon an increase in the local Ca^{2+} concentration. More specifically, the fast synaptic vesicle fusion requires Ca^{2+} concentrations in the range of tens to hundreds micromolar. In binding assays with negatively charged membranes, this concentration range corresponds to the relative Ca^{2+} affinity of the two C2 domains of synaptotagmin 1, the hypothesized Ca^{2+} sensor for this process. In solution, the Ca^{2+} binding affinity of these C2 domains is significantly lower compared with their relative affinity in the presence of membranes (12). This difference has been explained by a Ca^{2+}-bridging mechanism underlying these interactions. According to this hypothesis, the incomplete Ca^{2+} coordination sphere in the C2 domains is filled by phosphate groups of the phospholipids, resulting in complete coordination spheres of the C2 domain-bound Ca^{2+} ions and thus in a tremendous increase in the apparent Ca^{2+} affinity (13).

The C2 core domain is defined by the typical eight-stranded β-sandwich fold. Many C2 core domains contain also a Ca^{2+}-binding region (CBR)[5] with a conserved consensus sequence of acidic residues, but this motif alone does not reflect the large

* This work was supported in part by the Max Planck Society. The costs of publication of this article were defrayed in part by the payment of page charges. This article must therefore be hereby marked "*advertisement*" in accordance with 18 U.S.C. Section 1734 solely to indicate this fact.

[S] The on-line version of this article (available at http://www.jbc.org) contains supplemental Figs. 1–11 and Tables 1–4.

The atomic coordinates and structure factors (code 2CM5 and 2CM6) have been deposited in the Protein Data Bank, Research Collaboratory for Structural Bioinformatics, Rutgers University, New Brunswick, NJ (http://www.rcsb.org/).

[1] Both authors contributed equally to this work.

[2] Supported by Emmy Noether Grant ZW 71/1-5 from the Deutsche Forschungsgemeinschaft.

[3] Supported by the Fonds der Chemischen Industrie.

[4] To whom correspondence should be addressed: Dept. of NMR-based Structural Biology, Max Planck Institute for Biophysical Chemistry, Am Faßberg 11, 37077 Göttingen, Germany. Tel.: 49-551-201-2222; Fax: 49-551-201-2202; E-mail: sabe@nmr.mpibpc.mpg.de.

[5] The abbreviations used are: CBR, Ca^{2+}-binding region; SeMet, selenomethionine; HSQC, heteronuclear single quantum correlation; CBL, Ca^{2+}-binding loop; PS, phosphatidylserine.

variations in the Ca^{2+} and Ca^{2+}-mediated membrane binding affinities among these domains (14–16). These differences require subtle (14) or major (17) structural rearrangements. So far, such structural changes have been identified only within the C2 core domains of these proteins.

The Ca^{2+} binding mode of the C2B domain of rabphilin-3A has not been studied so far at atomic resolution. Its intrinsic Ca^{2+} binding affinity in solution has been shown to be in the 8–11 μM range (18). Based on the NMR structure of the C2B core domain, this unusually high Ca^{2+} affinity in comparison with C2 domains with a similar fold but much lower intrinsic Ca^{2+} affinity could not be explained. We took advantage of complementary x-ray and NMR techniques to probe the structural basis of this fundamental feature. The structural work presented here shows that Ca^{2+} binding of the C2B domain of rabphilin-3A is not mediated only by the classical CBR. Unexpectedly, a sequence upstream of the C2 core domain that belongs to the C2A-C2B tandem linker participates in the Ca^{2+} binding. This has important implications for the high intrinsic Ca^{2+} binding affinity of the C2B domain, the spatial proximity of the C2 domains upon Ca^{2+} signaling, and the way rabphilin-3A may interact with biological membranes.

EXPERIMENTAL PROCEDURES

Protein Expression and Purification—The cDNAs encoding fragments 371–510, 528–684, 519–684, and 371–684 of rat rabphilin-3A were cloned into the expression vector pGEX2T (Amersham Biosciences). The expression constructs encoding N-terminal glutathione *S*-transferase fusion proteins of these rabphilin-3A fragments were expressed and purified as described (19). Briefly, protein expression was carried out overnight in LB medium at 17 °C. The glutathione *S*-transferase fusion protein was purified on glutathione-Sepharose resin. Cleavage of the fusion protein was performed with thrombin on a column. The fragment released was further purified on a HiTrap SP XL cation exchange column (Amersham Biosciences). Fragment 519–684, used for crystallization experiments, was further purified by gel filtration on a Sephadex S-75 16/60 column (Amersham Biosciences). Selenomethionine (SeMet)-labeled protein was expressed in minimal medium supplemented with SeMet according to the EMBL Protein Expression Group (embl-heidelberg.de) and purified according to the established protocol.

The C2B domain single mutants E529A and E530A, double mutant E529A/E530A, and triple mutant E528A/E529A/E530A were obtained using the Stratagene QuikChange site-directed mutagenesis kit. The sense primers were designed as follows: E529A, 5′-ATG GCT CTC TAT GAG GCG GAG CAG GTG GAG C-3′; E530A, 5′-ATG GCT CTC TAT GAG GAG GCG CAG GTG GAG C-3′; E529A/E530A, 5′-ATG GCT CTC TAT GAG GCG GCG CAG GTG GAG C-3′; and E528A/E529A/E530A, 5′-ATG GCT CTC TAT GCG GCG GCG CAG GTG GAG-3′.

Crystallization and Structure Determination—For crystallization, rabphilin-3A fragment 519–684 was concentrated to 20 mg/ml. Crystals were obtained at 12 and 20 °C using vapor diffusion by mixing equal volumes of protein and reservoir solution (0.1 M HEPES (pH 8.5), and 20% polyethylene glycol monomethyl ether 2000 or 20% polyethylene glycol 8000). They grew within 1 week to a final size of $\sim 25 \times 25 \times 100\ \mu m^3$ and were used for streak seeding to obtain crystals of SeMet protein as well as crystals of native protein with reservoir solutions containing 200 mM Ca^{2+}. For data collection, all crystals were harvested and flash-frozen in liquid nitrogen in a cryosolution containing the reservoir solution supplemented with 10% glycerol. Data were collected at Swiss Light Source beamline PX6 (Mar225 CCD detector) and processed using the program HKL2000 (20). Statistics for data collection and processing are summarized in Table 1. The structure of crystals grown without adding Ca^{2+} was solved from SeMet crystals (space group $P2_12_12$) by multiwavelength anomalous dispersion phasing using the programs SHELXC, SHELXD, and SHELXE (21, 22). The initial electron density map was excellent (supplemental Fig. 1) and allowed automatic model tracing, alternated with structure refinement by ARP/wARP (23), resulting in the modeling of 131 residues. Refinement was performed by manual model building with COOT (24), followed by positional and *B*-factor refinement with REFMAC5 (25) coupled with ARP solvent building. For placing hydrogen atoms and refining occupancies due to radiation damage, the final refinement was done with SHELXL (26). The final model contains 143 of 165 residues, two Ca^{2+} ions, and 68 water molecules. Residues at the N terminus (positions 519–523) and C terminus (positions 578–584) and in two loop regions (positions 536–538 and 587–588) are disordered. The structure of crystals grown in Ca^{2+} (space group $P2_1$) was solved by molecular replacement with the program PHASER (27) using the SeMet structure as the search model. There are two monomers in the asymmetric unit. After initial rigid body and restrained *B*-factor refinement with REFMAC5 (25), manual model building was performed with COOT (24). The final refinement was done with SHELXL (26). The model contains 149 residues for monomer A, 147 residues for monomer B, one phosphate group, two Ca^{2+} ions for each monomer, and a total of 77 water molecules. In both monomers, residues at the N and C termini are disordered (monomer A, residues 519–523 and 679–684; and monomer B, residues 519–524 and 678–684). In monomer A, loop residues 536–538 and 587–588 are also disordered, whereas in monomer B, only loop residues 533–538 are disordered. The phosphate group forms a hydrogen bond with the backbone NH of Phe^{612} in monomer B and with Gly^{652} of a symmetry-related monomer B.

For both crystal structures, residues with completely or partially disordered side chains are listed in supplemental Tables 1 and 2. The statistics of the Ramachandran plots and of the refinement are shown in Table 1.

NMR Measurements—NMR experiments were carried out using a Bruker 700 or 900 spectrometer at 298 K. NMR samples for C2B domain fragments 519–684 and 528–684 and the C2A domain fragment (371–510) contained 1 mM ^{15}N- or $^{15}N/^{13}C$-uniformly labeled protein in 50 mM HEPES (pH 7.0), 150 mM NaCl, 1 mM dithiothreitol, and 10% D_2O (NMR buffer). The C2A-C2B domain (residues 371–684) samples contained 0.3 mM ^{15}N-labeled protein in NMR buffer. The Ca^{2+} concentrations added to the samples are specified below. Backbone C-α, C-β, and nitrogen chemical shifts were obtained using standard

TABLE 1
Data collection and refinement statistics

	Se PEAK	Se INFL	Se high remote	Native crystal with Ca^{2+}
Data collection				
Wavelength (Å)	0.9792	0.9796	0.9500	0.9536
Space group	$P2_12_12$	$P2_12_12$	$P2_12_12$	$P2_1$
Cell parameters (Å)		$a = 53.898$, $b = 60.043$, $c = 41.928$		$a = 40.069$, $b = 59.606$, $c = 66.385$ ($\beta = 103.89°$)
Resolution (Å)	1.91 (2.01-1.91)	1.92 (2.02-1.92)	1.28 (1.38-1.28)	1.85 (1.94-1.85)
Redundancy	7.07 (6.71)	6.17 (3.90)	1.72 (1.16)	6.44 (4.43)
Completeness (%)	98.6 (96.9)	96.9 (87.9)	94.2 (72.7)	97.2 (93.9)
Mean $I/\sigma(I)$	18.62 (12.89)	15.69 (7.74)	14.38 (2.84)	12.5 (3.07)
R_{int} (%)[a]	7.07 (12.90)	8.32 (14.84)	2.92 (21.00)	8.86 (40.06)
Refinement				
R[b]		14.40		19.48
R_{free}[c]		19.37		26.75
Protein atoms		1123		2314
Heteroatoms		2		9
Water molecules		68		77
Mean B-value (Å^2)		18.985		28.618
Main chain		15.726		25.973
Side chains		22.027		31.210
Standard uncertainties				
Bond length (Å)		0.011		0.005
Bond angle		0.030°		0.021°
Ramachandran plot (%)				
Most favored region		89.6		87.7
Allowed region		10.4		11.5
Generally allowed region		0		0.4
Disallowed region		0		0.4

[a] $R_{int} = \Sigma|F_o^2 - F_o^2(\text{mean})|/\Sigma[F_o^2]$.
[b] $R = \Sigma||F_o| - |F_c||/\Sigma|F_o|$.
[c] R_{free} is the same as R, expect for a 5% subset of all reflections.

triple-resonance experiments (28). All spectra were processed using NMRPipe/NMRDraw (29) and analyzed using NMRView Version 5.0.4 (30) and Sparky (31). ^1H-^{15}N nuclear Overhauser effect values were calculated as the intensity ratios of the ^1H-^{15}N correlation peaks from pairs of interleaved spectra acquired with and without ^1H saturation during the recycle time of 5 s (32).

The phospholipid binding assays were performed based on ^1H-^{15}N heteronuclear single quantum correlation (HSQC) spectra of 0.5–1 mM ^{15}N-labeled protein samples in NMR buffer. Liposomes were prepared from synthetic 1,2-dioleoyl-*sn*-glycero-3-phospho-L-serine and 1,2-dioleoyl-*sn*-glycero-3-phosphocholine (Avanti Polar Lipids) as follows. 1,2-Dioleoyl-*sn*-glycero-3-phospho-L-serine and 1,2-dioleoyl-*sn*-glycero-3-phosphocholine were dissolved at a molar ratio of 20:80 in chloroform/isopropyl alcohol (95:5, v/v). The lipid film obtained after overnight drying under vacuum was resuspended in 50 mM HEPES (pH 7.0) and 150 mM NaCl. After sonication, the lipid solution was passed 17 times through a 400-nm pore size filter using an extruder device (LiposoFast, Avestin Inc.). This liposome solution was added to the NMR sample to a final lipid concentration of 10 mM, resulting in a 3-fold molar excess of 1,2-dioleoyl-*sn*-glycero-3-phospho-L-serine to the protein.

A stock solution of 50 mM 1,2-dihexanoyl-*sn*-glycero-3-phospho-L-serine (Avanti Polar Lipids) in 50 mM HEPES (pH 7.0) and 150 mM NaCl was used to perform a titration with ^{15}N-labeled C2B domain fragment 519–684 in the presence of 0.1 mM Ca^{2+}. Glycerophosphoserine was chemically synthesized according to patent WO 87/05024 (42). A 100 mM glycerophosphoserine stock solution in 50 mM HEPES (pH 7.0) and 150 mM NaCl with 0.1 or 1 mM Ca^{2+} was used to perform titrations with 1 mM ^{15}N-labeled C2B domain fragment 519–684 NMR samples.

RESULTS

Overall Structure—The fragment chosen for crystallizing rabphilin-3A C2B domain fragment 519–684 was N-terminally extended by 5 residues compared with the fragment that had been used to solve the NMR structure of this C2B domain (fragment 524–684) (18). Using synchrotron radiation, native and SeMet crystals grown without the addition of Ca^{2+} diffracted up to 1.58- and 1.28-Å resolution, and native and SeMet crystals grown in the presence of 200 mM Ca^{2+} diffracted up to 1.91- and 1.85-Å resolution, respectively. Therefore, the structure of the crystals obtained without the addition of Ca^{2+} (low Ca^{2+} structure) was solved by multiwavelength anomalous dispersion using the SeMet crystals. This structure was used as a search model to obtain the structure of the native crystals grown with 200 mM Ca^{2+} in the reservoir (high Ca^{2+} structure) by molecular replacement. Under low Ca^{2+} conditions, the C2B domain fragment crystallized in space group $P2_12_12$ with one monomer in the asymmetric unit, whereas the presence of 200 mM Ca^{2+} in the reservoir resulted in crystals in space group $P2_1$ with two monomers in the asymmetric unit. As already described for its solution structure (18), the core of the C2B domain folds as a typical type I antiparallel eight-stranded β-sandwich with a short helix between strands 5 and 6 and a longer helix between strands 7 and 8 in both crystal structures (Fig. 1, *A* and *B*; and supplemental Fig. 2). It strongly resembles the structure in solution (root mean square deviations of 1.2909 Å with the low Ca^{2+} structure and 1.2386 and 1.2603 Å with monomers A and B of the high Ca^{2+} structure, respectively) (supplemental Fig. 3). Two Ca^{2+} ions are bound in the low as

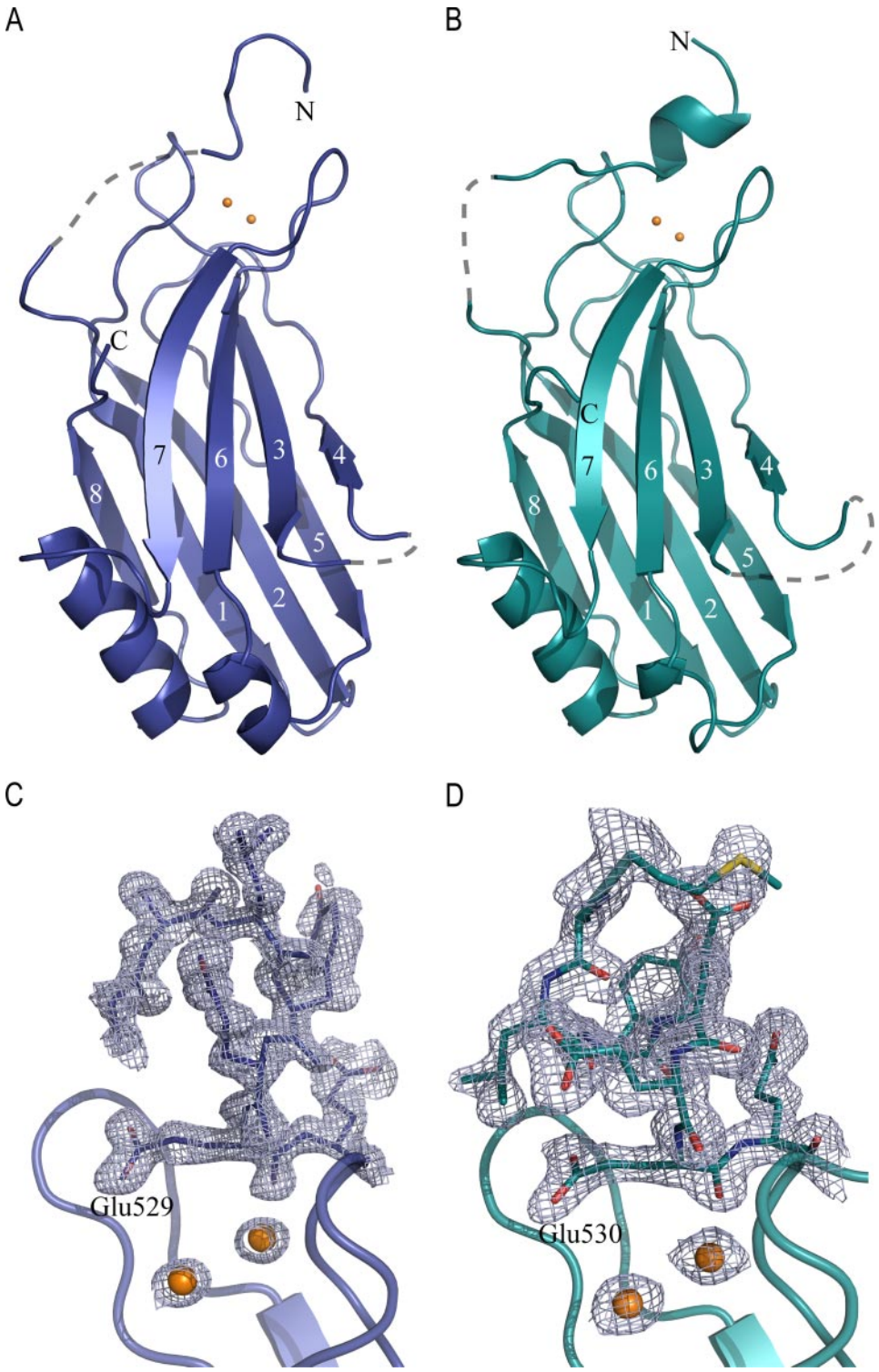

FIGURE 1. **Structure of rabphilin-3A C2B domain fragment 519–684.** *A*, ribbon model of the low Ca^{2+} ($P2_12_12$) structure. The Ca^{2+} ions are presented as *orange spheres*. All structural figures were generated with PyMOL (pymol.sourceforge.net). *B*, ribbon model of monomer A (*green*) of the high Ca^{2+} structure ($P2_1$). *C* and *D*, $2mF_o - DF_c$ electron density maps of the linker region in the low and high (monomer A) Ca^{2+} structures, respectively.

well as high Ca^{2+} structure. This is in accordance with the surprisingly high Ca^{2+} binding affinity described for this C2 domain in solution (18). An unexpected feature is found in both crystal structures: several residues from the region upstream of the core domain (residues 519–549) interact with the CBR of the C2 domain (Fig. 1, *C* and *D*). In rabphilin-3A, this region is part of the linker between the C2A and C2B domains. More specifically, a stretch of 6 residues (Leu^{526}–Gln^{531}) docks to the region between Ca^{2+}-binding loop (CBL) 1 and CBL3, thus forming a lid above the Ca^{2+}-binding sites. The secondary structure of this short stretch differs between the two crystal structures. In the low Ca^{2+} structure, it forms an extended loop, whereas in the high Ca^{2+} structure, it forms a short helix. Despite differences in hydrogen bonding to symmetry-related molecules (supplemental Tables 3 and 4), the two structures obviously represent two possible conformations in which the N-terminal acidic region may contribute to Ca^{2+} binding. The loop connecting this N-terminal part of the linker region to β-strand 1 of the C2 core domain is partially disordered (Fig. 1, *A* and *B*; and supplemental Fig. 2).

The C2A-C2B Linker Is Involved in Ca^{2+} Binding—In both crystal structures, a glutamic acid residue establishes essential contacts with CBL3 and with both Ca^{2+} ions. This residue is Glu^{529} in the low Ca^{2+} structure and Glu^{530} in the high Ca^{2+} structure. Despite the different secondary structures in the N-terminal stretch, in both structures, these glutamic acid residues are in a nearly identical position and orientation relative to the Ca^{2+}-binding sites and to CBL3 (Figs. 1, *C* and *D*; and 2*B*). They interact with the Ca^{2+} in binding site 2 through their main chain carbonyl groups and contact the Ca^{2+} in binding site 1 through water-mediated hydrogen bonding of their O-ϵ2. Otherwise, both Ca^{2+} ions interact with the acidic residues found in the classical consensus sequence (13) of C2 domains (Fig. 2, *A* and *B*). The Ca^{2+} in binding site 2 is coordinated by the main chain carbonyl group of Met^{570}; the O-δ1 of Asp^{571} and Asp^{633}; the O-δ2 of Asp^{631}, Asp^{633}, and Asp^{639}; and the already mentioned carbonyl group of the Glu^{529}/Glu^{530} backbone. The Ca^{2+} in binding site 1 is coordinated by the main chain carbonyl of Tyr^{632}; the O-δ1 of Asp^{571}, Asp^{631}, and Asp^{633}; and the O-δ2 of Asp^{571} and Asp^{577}. The seventh oxygen atom is pro-

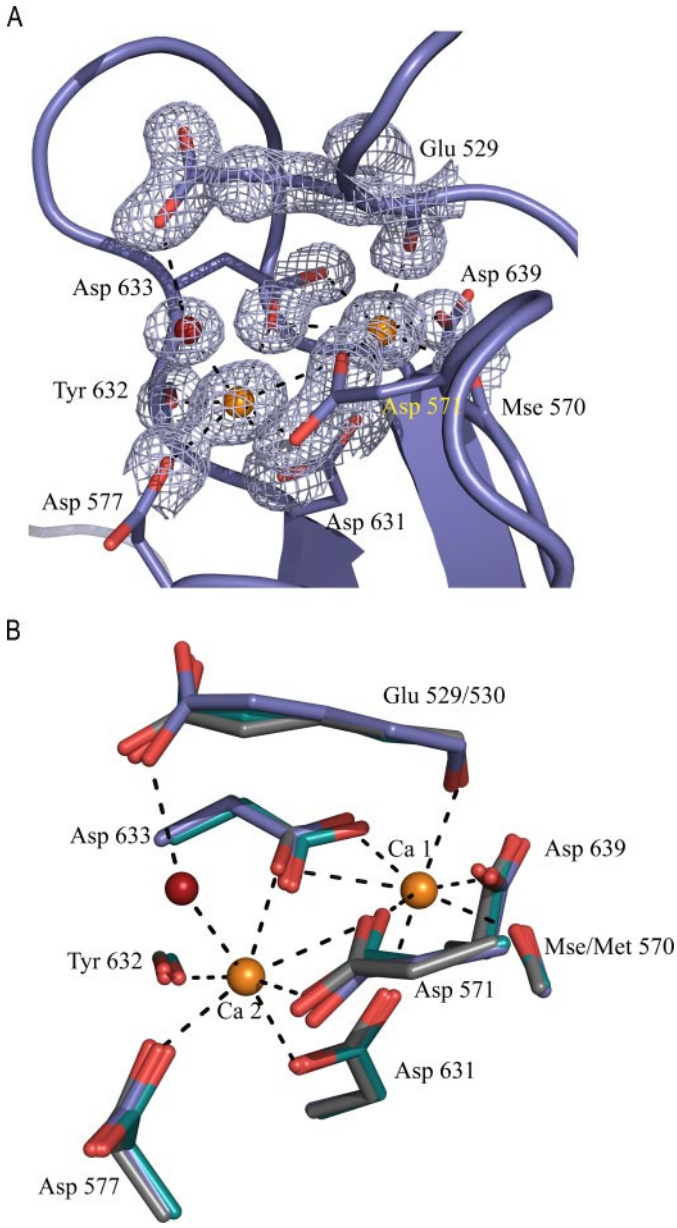

FIGURE 2. **Coordination of the Ca^{2+} ions in the C2B domain of rabphilin-3A.** *A*, electron density ($2mF_o - DF_c$ map) in the CBR of the low Ca^{2+} structure. *Mse*, selenomethionine. *B*, superposition of the side chains of the coordinating residues of both crystal structures. The low Ca^{2+} structure is colored in *blue*; monomer A of the high Ca^{2+} structure in shown in *cyan* and monomer B in *gray*. The Ca^{2+} ions are depicted in *yellow*, and the water molecule coordinating to the Ca^{2+} in binding site 2 (*Ca 2*) is shown in *orange*.

vided by the only Ca^{2+}-coordinating water molecule, which hydrogen bonds with the side chain O-ϵ2 of Glu^{529}/Glu^{530} (Fig. 2, *A* and *B*). Thus, both Ca^{2+} ions are heptacoordinate with a pentagonal bipyramidal coordination geometry, which recalls the one found in EF-hand proteins (supplemental Fig. 4). The water molecule that participates in the coordination sphere of the Ca^{2+} in binding site 1 as the seventh ligand interacts extensively with several Ca^{2+}-binding residues belonging to the consensus sequence, *viz.* the O-δ2 of Asp^{571}, the O-ϵ2 of Glu^{530}, the O-δ2 of Asp 577, and the O-δ1 of Asp^{633}. In both crystal structures, the side chain carboxyl group of Glu^{529}/Glu^{530} forms additional hydrogen bonds with the backbone NH groups of Ile^{634} and Gly^{635}, thus securing a strong interaction between the N-terminal linker region and CBL3. Next to the Ca^{2+}-bridging Glu^{529}/Glu^{530} residue, Glu^{528}/Glu^{529} (in low *versus* high Ca^{2+} structures) establishes, through its backbone carbonyl group, a hydrogen bond with the Ala^{572} main chain amide, holding CBL1 tightly packed in the CBR. Thus, in both crystal structures, the first of the two acidic patches from the linker (see Fig. 6) connects CBL1 and CBL3 through a hydrogen bond network (Fig. 3, *A* and *B*).

Another striking feature concerns the positioning of the Lys^{636} side chain, which interacts via hydrogen bonds with two Ca^{2+}-binding residues, *viz.* Asp^{633} O-δ1 and Asp^{639} O-δ2 (Fig. 3, *A* and *B*). This has two consequences. First, the motions of the side chains of both Ca^{2+}-binding residues may be restricted, holding them in an optimal position for binding the Ca^{2+} ions. Second, the positive charge carried by the side chain amino group of Lys^{636} is spatially located at the same position as the third Ca^{2+}-binding site found in the C2A domain of synaptotagmin 1 (Fig. 3*C*).

Acidic Residues from the Linker Are Essential for the High Ca^{2+} Binding Affinity of the C2B Domain—To further investigate the interaction of the C2A-C2B domain linker region with the C2B core domain, we performed a solution NMR study. For this purpose, two C2B domain fragments were produced: a "long" fragment (residues 519–684), used to crystallize this domain, and a "short" fragment (residues 528–684), including the first acidic patch (see Fig. 6). Experiments to obtain C2B core domain fragment 541–684 in soluble form failed. Additionally, we also performed NMR measurements on the C2A-C2B tandem (residues 371–684) and C2A domain (residues 371–510) fragments.

Triple-resonance backbone assignment experiments were carried out on C2B domain fragment 519–684. Of the 22 residues of linker region 519–540, Arg^{522}–Tyr^{527} and Glu^{533}–Glu^{539} could be assigned (supplemental Fig. 5*A*). The assigned residues belong to the flexible parts of the N-terminal linker, *i.e.* the disordered (non-core domain-interacting) residues in the crystal structure. To address the flexibility of these residues, we measured their ^1H-^{15}N heteronuclear nuclear Overhauser effect values. From Met^{524} on, the nuclear Overhauser effect intensity ratios of 0.5 (supplemental Fig. 6) indicate restricted motions for the linker. The missing residues, including the first acidic patch (positions 528–530), are probably involved in chemical exchange on an intermediate time scale. This chemical exchange may be related to the acidic residue switch observed between the low and high Ca^{2+} crystal structures (Figs. 1, *C* and *D*; and 2*B*).

Because of the spectral broadening of the cross-peaks corresponding to the residues defining the first acidic patch (Glu^{528}–Val^{532}), we indirectly observed the localization of the N-terminal linker on the C2B core domain. Analysis of the ^1H-^{15}N HSQC spectra of fragments 519–684 and 528–684 (supplemental Fig. 7, *A* and *B*) showed chemical shift differences between both fragments mainly for residues in CBL1–3. Moreover, the peak intensity ratios in the HSQC spectra of fragment 528–684 compared with fragment 519–684 illustrate an increase in intensity of the cross-peaks corresponding to the backbone HN of the residues located in CBL3 (positions 632–

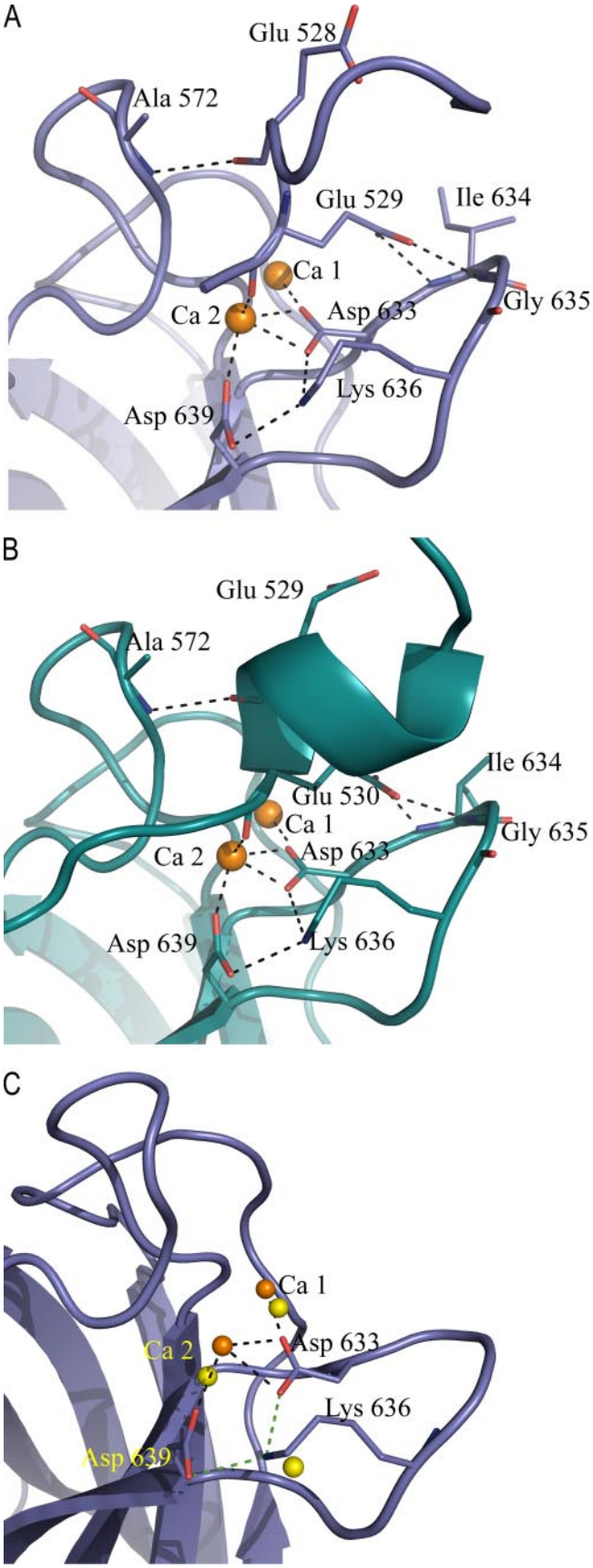

FIGURE 3. **Interaction network between the linker region and the CBLs.** *A*, low Ca^{2+} structure; *B*, high Ca^{2+} structure; *C*, superposition with the Ca^{2+} ions of the synaptotagmin 1 C2A domain (Protein Data Bank code 1BYN; in *yellow*). For clarity, the N-terminal linker region is not shown. Hydrogen bonds involving Lys^{636} are depicted in *green*. *Ca 1* and *Ca 2*, Ca^{2+} in binding sites 1 and 2, respectively.

638) and of Lys^{601} in CBL2. In addition, the shortening of the linker affects the disordered C-terminal tail of the C2B domain as well as the last linker residues (supplemental Fig. 7, *A* and *B*). It is noteworthy that the residues preceding the N-terminal β-strand of the C2B core domain (the last linker residues) are in close proximity to the residues following the last β-strand of the core domain in the crystal structures (Fig. 1, *A* and *B*). These observations are topologically in agreement with the orientation of the linker seen in the crystal structures with respect to the CBR.

To confirm the interaction of Glu^{529} and Glu^{530} with the Ca^{2+}-binding region of the C2B domain, four mutants (E529A, E530A, E529A/E530A, and E528A/E529A/E530A) were produced. ^{15}N-^{1}H HSQC-based Ca^{2+} titrations performed on these mutants showed that they were still able to bind Ca^{2+}. Whereas the single mutants were saturating at 0.5 mM Ca^{2+}, the double and triple mutants required 2 mM Ca^{2+} to reach the saturation point. In the Ca^{2+}-bound state, the resonances of residues from all three CBLs were affected in each of these mutants (supplemental Fig. 8). This observation is in agreement with the crystal structures and confirms that the linker binds to the Ca^{2+}-loaded CBR in solution. In contrast, the overlay of the ^{1}H-^{15}N HSQC spectra of these mutants in the presence of 10 mM EGTA with the wild-type Ca^{2+}-free C2B domain shows no significant perturbation for the core domain residues (supplemental Fig. 9*A*). This indicates that the linker binds to the CBR only in the presence of Ca^{2+}.

The chemical shift deviation of cross-peaks from several residues of the double mutant (E529A/E530A) and the triple mutant (E528A/E529A/E530A) can be followed by ^{1}H-^{15}N HSQC-based Ca^{2+} titration. Six residues show chemical shift deviations in the fast exchange regime for these mutants. A simultaneous fit using the Hill equation led to a dissociation constant (K) of 101 $\pm$ 25 μM with a Hill coefficient (n_H) of 1.45 $\pm$ 0.19 for the E529A/E530A mutant and K = 116 $\pm$ 22 μM with n_H = 1.50 $\pm$ 0.08 for the E528A/E529A/E530A mutant (supplemental Fig. 10). The overlay of the ^{1}H-^{15}N HSQC spectra of both mutants in the Ca^{2+}-bound state shows identical chemical shifts for cross-peaks of the core domain residues (supplemental Fig. 9*B*). This indicates that Glu^{528} does not interact with the CBR when Glu^{529} and Glu^{530} are mutated to alanine. Thus, mutating the crucial residues Glu^{529} and Glu^{530} to alanine leads to a 10-fold decrease in the intrinsic Ca^{2+} binding affinity of the C2B domain. Although not seen in the crystal structures, the C-terminal residues are strongly affected by the mutations, suggesting an interaction of these residues with the N-terminal linker residues in the CBR-bound state.

The Ca^{2+} Binding Mode of the C2B Domain Is Maintained in the C2 Domain Tandem Fragment—The overlay of the ^{1}H-^{15}N HSQC spectra of C2B domain fragment 519–684 and the C2A-C2B tandem fragment (residues 371–684) in the presence of 5 mM Ca^{2+} shows a very good match of the cross-peaks corresponding to the core domain residues as well as the linker residues that are included in C2B domain fragment 519–684 (Fig.

4*A*). In the tandem fragment, the relative intensities of the cross-peaks from the linker residues compared with those from the core domain residues are similar to the ratios obtained for C2B domain fragment 519–684. In addition, well resolved cross-peaks from the residues of the linker show similar chemical shift deviations upon Ca^{2+} binding compared with C2B domain fragment 519–684 (supplemental Fig. 11). These observations suggest that the interaction of the linker with the CBR in the isolated C2B domain is maintained in the C2 domain tandem fragment.

We also probed the Ca^{2+} binding properties of the C2B domain in the C2A-C2B tandem fragment (residues 371–684). 5 mM Ca^{2+} in the NMR buffer was needed to obtain a fully Ca^{2+}-loaded C2A domain fragment (residues 371–510) (Fig. 4*B*), whereas it stayed in the Ca^{2+}-free state in the presence of 0.1 mM Ca^{2+}, as verified by comparison with the HSQC spectrum in the presence of 10 mM EGTA. On the other hand, C2B domain fragment 519–684 was in its Ca^{2+}-loaded state in the presence of 0.1 and 5 mM Ca^{2+}. Its intrinsic high Ca^{2+} binding affinity led to the purification of the Ca^{2+}-bound form anyway. Therefore, no further chemical shift deviations could be observed in the HSQC spectra of this domain when NMR buffer was supplemented with 0.1 or 5 mM Ca^{2+}. We then compared the Ca^{2+}-loaded state of both domains in the C2A-C2B tandem fragment in the presence of these two Ca^{2+} concentrations. In buffer containing 0.1 mM Ca^{2+}, the C2B domain in this fragment was in the Ca^{2+}-bound form, whereas the C2A domain remained Ca^{2+}-free (Fig. 4*B*). In the presence of 5 mM Ca^{2+}, both domains were in the Ca^{2+}-loaded state. This indicates that the high affinity Ca^{2+} binding property of the C2B domain is maintained in the C2 domain tandem fragment probably because of the interaction of the acidic linker residues with the C2B domain.

Upon Interaction with Phospholipid Bilayers, the Linker Stays Bound to the CBR—The coordination spheres of the Ca^{2+} ions in the crystal structures of C2B domain fragment 519–684 almost completely consist of protein oxygen atoms; there is just one metal-bound water molecule (Fig. 2*B*). According to the Ca^{2+}-bridging phospholipid binding model, only one binding site is left for an anionic phospholipid head group if the linker remains on the CBR once the protein is bound to the membrane. This structural feature, unusual for a C2 domain, raises the question of the Ca^{2+}-dependent phospholipid-binding mechanism of this domain. We used NMR spectroscopy as a tool to assay the binding mode of the C2B domain to soluble phosphatidylserine (PS) and PS-containing liposomes. The PS head group-specific recognition has been addressed using soluble glycerophosphoserine and 1,2-dihexanoyl-*sn*-glycero-3-phospho-L-serine. Neither a 20-fold excess of glycerophosphoserine nor subcritical micellar concentrations of 1,2-dihexanoyl-*sn*-glycero-3-phospho-L-serine induced any significant chemical shift perturbation or peak intensity change in the CBR of the C2B domain. Concentrations of 1,2-dihexanoyl-*sn*-glycero-3-phospho-L-serine above the critical micellar concentration (1.1 mM) induced an overall broadening of all cross-peaks of the C2B domain spectra. Consequently, as for most C2 domains that bind PS in a Ca^{2+}-dependent fashion, no specific PS head group-binding site could be observed.

Next, binding to phospholipid bilayers was probed by a ^{1}H-^{15}N HSQC-based Ca^{2+} titration starting with the Ca^{2+}-free C2B domain in the presence of 80:20 1,2-dioleoyl-*sn*-glycero-3-phosphocholine/1,2-dioleoyl-*sn*-glycero-3-phospho-L-serine liposomes. Although C2B domain fragments 519–684 and 528–684 were expressed and purified without adding Ca^{2+} to any buffers, the HSQC spectra showed that, for both fragments, the C2B domains were in the Ca^{2+}-bound form. The removal of the Ca^{2+} ions by the addition of 10 mM EGTA affected also the chemical shift of most of the residues belonging to the linker (Fig. 5*C*). It is noteworthy that new highly intense cross-peaks appeared in the Ca^{2+}-free ^{1}H-^{15}N HSQC spectrum of the C2B domain and were localized in a narrow region of the spectrum characteristic for non-structured residues (Fig. 5*C*). These signals have been assigned (supplemental Fig. 5*B*) to the N-terminal linker residues that are in chemical exchange at an intermediate time scale in the presence of Ca^{2+}. Moreover, the heteronuclear ^{1}H-^{15}N nuclear Overhauser effect values of the linker residues were reduced in the Ca^{2+}-free form compared with the Ca^{2+}-bound form (data not shown). Taken together with the data related to the E529A and E530A mutants, these observations show that the linker is more flexible in the absence of Ca^{2+}.

The Ca^{2+}-free C2B domain was not able to bind to liposomes. The addition of increasing amounts of Ca^{2+} triggered the binding of the C2B domain to the liposomes, as monitored by the broadening of almost all of the ^{1}H-^{15}N cross-peaks (Fig. 5*A*). The only remaining cross-peaks belonged to the flexible residues from the N-terminal linker (Fig. 5*A*). The chemical shifts of these residues were almost identical to those observed in the Ca^{2+}-bound form in solution (Fig. 5*A*). Moreover, the intense cross-peaks observed in the Ca^{2+}-free C2B domain spectrum, assigned to the acidic residues of the linker (supplemental Fig. 5*B*), were not seen in the liposome-bound form of the C2B domain (Fig. 5, *B* and *C*). This suggests that the binding to the liposomes does not trigger the release of the linker. These observations strongly indicate that the structural features previously observed for the CBR of the C2B domain in the presence of Ca^{2+} are maintained in the membrane-bound state.

DISCUSSION

The C2A-C2B Linker Modulates the Ca^{2+} Binding Affinity of the C2B Domain—A recent study performed on a rabphilin-3A knock-out mouse attributed, for the first time, a specific function to the C2B domain of this protein in the repriming of vesicles following induced vesicle fusion (8). This process takes place at residual Ca^{2+} concentrations and probably requires the interaction with SNAP25. The high affinity Ca^{2+} binding mode is thus essential for the function of rabphilin-3A. Through investigation of this Ca^{2+} binding mode, we have shown in this work that a number of acidic residues from the C2A-C2B linker region that are not part of the C2B core domain interact with the Ca^{2+}-binding region of this domain. Because of these interactions, the coordination sphere of both Ca^{2+} ions is almost completely created by protein residues (Fig. 2, *A* and *B*). Most strikingly, these additional linker residues in the coordination sphere of the Ca^{2+} ions enable the formation of an exhaustive

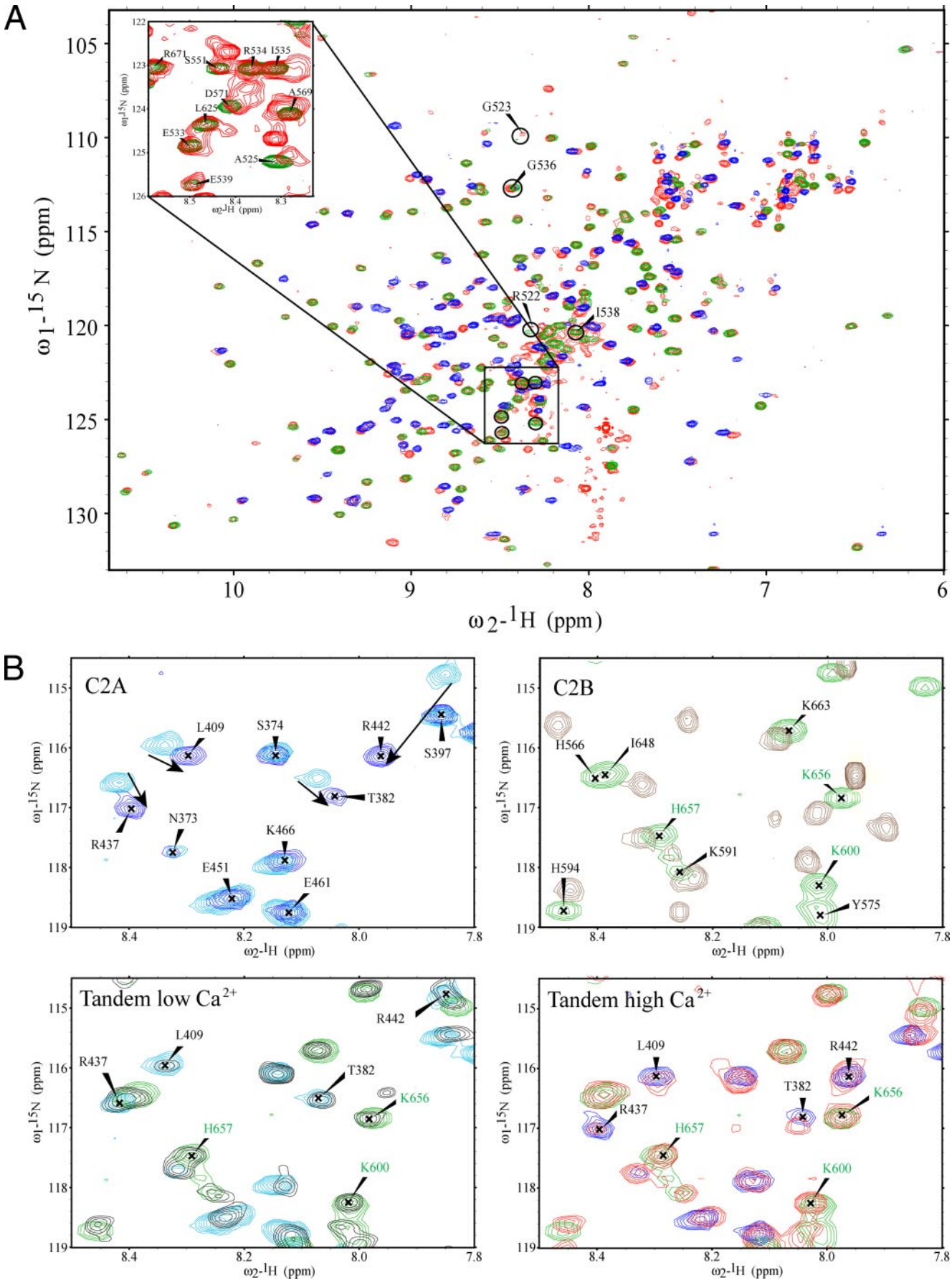

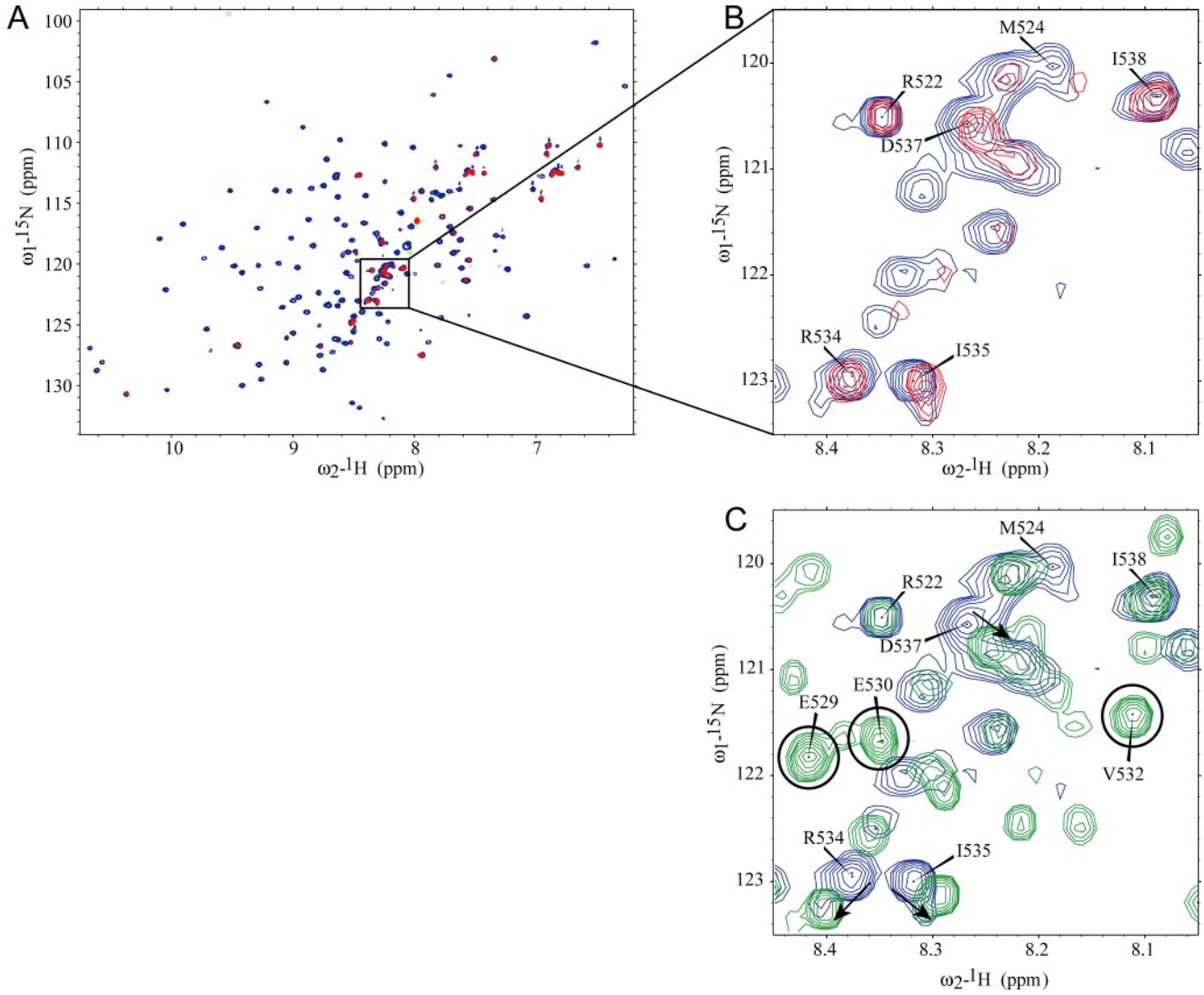

FIGURE 5. **Liposome binding assays of the C2B domain of rabphilin-3A.** *A*, overlay of the ^{1}H-^{15}N HSQC spectra of Ca^{2+}-bound C2B domain fragment 519–684 in the absence (*blue*) and presence (*red*) of liposomes. *B*, enlarged region of *A*. HN cross-peaks corresponding to linker residues are labeled. *C*, overlay of the ^{1}H-^{15}N HSQC spectra of Ca^{2+}-bound C2B domain fragment 519–684 (*blue*) and the Ca^{2+}-free C2B domain (*green*). Additional intense cross-peaks corresponding to residues from the acidic patch of the linker are *encircled*.

hydrogen bond network stabilizing CBL1 and CBL3 (Fig. 3, *A* and *B*). Two different acidic residues (Glu^{529} *versus* Glu^{530}) are involved in this extensive hydrogen bond network in the two crystal structures (Fig. 3, *A* and *B*), but their identical orientation relative to both Ca^{2+} ions suggests that the architecture of the whole interaction network is energetically highly favorable. It is noteworthy that the Lys^{636} side chain amino group establishes two hydrogen bonds with both Ca^{2+}-coordinating carboxylic groups of Asp^{633} and Asp^{639} (Fig. 3*C*). This interaction allows the Asp^{639} side chain to participate with the Ca^{2+} in binding site 2 in our crystal structures, contrary to the equivalent residue Asp^{371} in synaptotagmin 1 C2B domain crystal structures (33). In addition, the Lys^{636} side chain amino group may well mimic, in terms of charge distribution, Ca^{2+}-binding site IV found in the C2A domain of synaptotagmin 1 and protein kinase Cδ (34, 35). This may be important for the phospholipid binding mode of the C2B domain of rabphilin-3A by constituting an additional localized PS-binding site. Thus, the CBR

FIGURE 4. **The C2B domain in the rabphilin-3A C2A-C2B tandem fragment (residues 371–684) shows high intrinsic Ca^{2+} affinity.** *A*, overlay of the ^{1}H-^{15}N HSQC spectra of the C2A-C2B tandem fragment (residues 371–684; *red*), the C2B domain alone (residues 519–684; *green*), and the C2A domain alone (residues 371–510; *blue*) in the presence of 5 mM Ca^{2+}. Well resolved ^{1}H-^{15}N cross-peaks from the N-terminal part of the C2B domain (residues 519–684) found in the C2A-C2B tandem fragment are *encircled*. The *inset* shows an overlay of a region of the C2A-C2B tandem fragment (*red*) and the C2B domain (*green*). Cross-peaks of linker residues (Arg^{522}, Gly^{523}, Ala^{525}, Glu^{533}, Arg^{534}, Ile^{535}, Ile^{538}, and Glu^{539}) are labeled. *B*, overlays of ^{1}H-^{15}N HSQC spectra. *Upper left panel*, C2A domain (residues 371–510). *Turquoise*, 10 mM EGTA; *blue*, 5 mM Ca^{2+}. The *arrows* indicate the chemical shift deviation induced by Ca^{2+}. Cross-peaks of the Ca^{2+}-loaded form are labeled. *Upper right panel*, C2B domain (residues 519–684). *Brown*, 10 mM EGTA; *green*, 5 mM Ca^{2+}. Cross-peaks of the Ca^{2+}-loaded form are labeled. The *green labels* are the ones reported in the *lower panels*. *Lower left panel*, C2A-C2B tandem fragment (residues 371–684) in 0.1 mM Ca^{2+}. *Black*, C2A-C2B tandem fragment; *turquoise*, C2A domain in 0.1 mM Ca^{2+}; *green*, C2B domain in 5 mM Ca^{2+}. *Black labels* correspond to cross-peaks from the C2A domain affected by Ca^{2+}, and *green labels* indicate cross-peaks from the C2B domain. *Lower right panel*, C2A-C2B tandem fragment (residues 371–684) in 5 mM Ca^{2+}. *Red*, C2A-C2B tandem fragment; *blue*, C2A domain in 5 mM Ca^{2+}; *green*, C2B domain in 5 mM Ca^{2+}.

FIGURE 6. **Acidic sequences found upstream of C2 core domains.** Shown is the sequence alignment of C2B domains (rabphilin-3A and Doc2γ) and C2A domains (rabphilin-3A; synaptotagmins (*SYT*) 7, 1, and 2; Doc2α; and Doc2β), including sequences upstream of the C2 core domains. All sequences are from *Rattus norvegicus*. The secondary structure elements correspond to the rabphilin-3A C2B core domain structures. *Black arrows* represent the β-strands, and *gray rectangles* represent the α-helices. The color code for the alignment is as follows: *dark green*, identical residues; *green*, similar residues; and *pale green*, blocks of similar residues. The alignment was performed using Vector NTI. The *red box* highlights the acidic sequences upstream of the C2 core domains, and the *orange boxes* show the two acidic patches (first patch, residues 528–530; and second patch, residues 537–540) in the rabphilin-3A C2A-C2B tandem linker. The consensus sequence is shown at the bottom of the alignment.

of the rabphilin-3A C2B domain structure provides the most optimal Ca^{2+}-binding site of any C2 domain structurally studied so far.

The double mutation of both glutamic acid residues (E529A/E530A) involved in the interaction with the CBR lowers the intrinsic Ca^{2+} binding affinity of C2B by a factor of 10. This shows that the acidic patch of the linker is directly responsible for the high Ca^{2+} binding affinity of the C2B domain. This unprecedented structural feature defining the high intrinsic Ca^{2+} binding affinity of the C2B domain suggests a role for this acidic patch in the response of the rabphilin-3A C2B domain to low physiological Ca^{2+} concentrations. In addition, as shown by NMR, the linker binds to the CBR of the C2B domain in the presence of Ca^{2+}, whereas it stays flexible in the Ca^{2+}-free state. This implies a more compact C2 domain tandem in the Ca^{2+}-bound state, which could be important for modulating the functional interplay between both C2 domains.

The C2A-C2B Linker Is Involved in Phospholipid Binding of the C2B Domain—The standard model for C2 domain-membrane interaction implies that the Ca^{2+} ions function as a bridge between the protein and the phospholipids. According to this model, the phosphate moiety of the phospholipids and the carboxylic moiety of the PS head group complete the coordination spheres of the Ca^{2+} ions. The Ca^{2+}-coordinating water molecules found in the various crystal structures of C2 domains are then displaced by the phospholipids, and no strong specific PS head group-protein interactions are required for the binding (34, 36, 37). This binding model agrees well with the low intrinsic Ca^{2+} affinity of these domains in solution compared with their higher relative Ca^{2+} binding affinity in the presence of membranes.

We could not identify a PS head group-specific binding site on the C2B domain of rabphilin-3A. This is suggestive of a Ca^{2+}-dependent, multiple ligand-driven binding mode. According to the standard C2 domain-membrane interaction model, the linker region would have to be released from the CBR upon binding to the membrane to partially free Ca^{2+} coordination sites. The binding of the C2B domain to phosphocholine/PS liposomes did not show any indications for such a switch in the HSQC spectra (Fig. 5). The interpretation of our NMR data rather suggests that the acidic linker residues involved in Ca^{2+} coordination stay bound to the CBR of the C2B domain upon phospholipid binding. Thus, the standard model for Ca^{2+}-mediated phospholipid binding by C2 domains is probably not applicable to this specific case. Instead, the unique structural motif arising from the interaction between the acidic linker residues and the CBR may constitute a new type of scaffold for Ca^{2+}-mediated protein-phospholipid interactions. Such an alternative phospholipid binding mode would probably require the emergence of new PS-binding sites defined by specific structural features of the linker-bound CBR. Further investigations, *e.g.* using the EPR membrane depth method (38), will be required to obtain a more detailed understanding of the C2B domain-membrane interaction at the molecular level.

What Is the Role of Acidic Motifs for other C2 Domains?—Among the C2 domain tandem proteins, this is, to our knowledge, the first case in which a sequence motif located in the linker connecting two C2 domains interacts with the Ca^{2+}-binding region of one of them. The sequence homology of these linkers is generally low, and their lengths are highly variable. Doc2γ (double C2 protein) is actually the only protein containing a C2 domain tandem fragment that shows high sequence similarity to rabphilin-3A in the linker region (39). No information on its possible function is available so far. Interestingly, such acidic patches are more generally found upstream of several C2A domains (Fig. 6). In light of our results, these specific sequences may have specific functions for the C2A domains. First, they may significantly affect the intrinsic Ca^{2+} binding property of these C2 domains. It has been shown that the C2A domains of Doc2α and Doc2β require a Ca^{2+} concentration in the low micromolar range to localize at the plasma membrane

in vivo (40). Similarly, synaptotagmin 7 binds phospholipids at low micromolar Ca^{2+} concentrations (41). Its C2A domain has the highest relative Ca^{2+} affinity for membrane binding of all synaptotagmin isoforms investigated so far (16). This suggests that the Ca^{2+} binding mode of these C2A domains may be similar to the Ca^{2+} binding mode observed for the C2B domain of rabphilin-3A in this study. Second, the binding of the linker to the C2B domain of rabphilin-3A in the presence of Ca^{2+} probably triggers a closer proximity of both C2 domains. In synaptotagmins, an acidic motif connects their transmembrane part and the first C2 domain. In Doc2α, such a motif connects the Munc13-1-interacting domain and the C2A domain. In analogy to rabphilin-3A, these acidic patches may be important to restrain the spatial localization of C2 domains to neighboring domains in the presence of Ca^{2+}. Further investigations will be required to address the functional involvement of such motifs in C2 domain tandem proteins.

Acknowledgments—We thank Kamila Budzyn for expert technical help, Christian Griesinger for useful discussions and generous support, and Ehmke Pohl and Anuschka Pauluhn for assistance with data collection.

REFERENCES

1. Coppola, T., Hirling, H., Perret-Menoud, V., Gattesco, S., Catsicas, S., Joberty, G., Macara, I. G., and Regazzi, R. (2001) *J. Cell Sci.* **114,** 1757–1764
2. Chung, S. H., Takai, Y., and Holz, R. W. (1995) *J. Biol. Chem.* **270,** 16714–16718
3. Arribas, M., Regazzi, R., Garcia, E., Wollheim, C. B., and De Camilli, P. (1997) *Eur. J. Cell Biol.* **74,** 209–216
4. Joberty, G., Stabila, P. F., Coppola, T., Macara, I. G., and Regazzi, R. (1999) *J. Cell Sci.* **112,** 3579–3587
5. Tsuboi, T., and Fukuda, M. (2005) *J. Biol. Chem.* **280,** 39253–39259
6. Schluter, O. M., Schnell, E., Verhage, M., Tzonopoulos, T., Nicoll, R. A., Janz, R., Malenka, R. C., Geppert, M., and Sudhof, T. C. (1999) *J. Neurosci.* **19,** 5834–5846
7. Staunton, J., Ganetzky, B., and Nonet, M. L. (2001) *J. Neurosci.* **21,** 9255–9264
8. Deak, F., Shin, O. H., Tang, J., Hanson, P., Ubach, J., Jahn, R., Rizo, J., Kavalali, E. T., and Sudhof, T. C. (2006) *EMBO J.* **25,** 2856–2866
9. Gonzalez, L., Jr., and Scheller, R. H. (1999) *Cell* **96,** 755–758
10. Fukuda, M., Kanno, E., and Yamamoto, A. (2004) *J. Biol. Chem.* **279,** 13065–13075
11. Chung, S. H., Song, W. J., Kim, K., Bednarski, J. J., Chen, J., Prestwich, G. D., and Holz, R. W. (1998) *J. Biol. Chem.* **273,** 10240–10248
12. Sudhof, T. C. (2004) *Annu. Rev. Neurosci.* **27,** 509–547
13. Rizo, J., and Sudhof, T. C. (1998) *J. Biol. Chem.* **273,** 15879–15882
14. Dai, H., Shin, O. H., Machius, M., Tomchick, D. R., Sudhof, T. C., and Rizo, J. (2004) *Nat. Struct. Mol. Biol.* **11,** 844–849
15. Shin, O. H., Maximov, A., Lim, B. K., Rizo, J., and Sudhof, T. C. (2004) *Proc. Natl. Acad. Sci. U. S. A.* **101,** 2554–2559
16. Sugita, S., Shin, O. H., Han, W., Lao, Y., and Sudhof, T. C. (2002) *EMBO J.* **21,** 270–280
17. Garcia, J., Gerber, S. H., Sugita, S., Sudhof, T. C., and Rizo, J. (2004) *Nat. Struct. Mol. Biol.* **11,** 45–53
18. Ubach, J., Garcia, J., Nittler, M. P., Sudhof, T. C., and Rizo, J. (1999) *Nat. Cell Biol.* **1,** 106–112
19. Fykse, E. M., Li, C., and Sudhof, T. C. (1995) *J. Neurosci.* **15,** 2385–2395
20. Otwinowski, Z., and Minor, W. (1997) *Methods Enzymol.* **276,** 307–326
21. Schneider, T. R., and Sheldrick, G. M. (2002) *Acta Crystallogr. Sect. D Biol. Crystallogr.* **58,** 1772–1779
22. Sheldrick, G. M. (2002) *Z. Kristallogr.* **217,** 644–650
23. Perrakis, A., Morris, R., and Lamzin, V. S. (1999) *Nat. Struct. Biol.* **6,** 458–463
24. Emsley, P., and Cowtan, K. (2004) *Acta Crystallogr. Sect. D Biol. Crystallogr.* **60,** 2126–2132
25. Murshudov, G. N., Vagin, A. A., and Dodson, E. J. (1997) *Acta Crystallogr. Sect. D Biol. Crystallogr.* **53,** 240–255
26. Sheldrick, G. M., and Schneider, T. R. (1997) *Methods Enzymol.* **277,** 319–343
27. McCoy, A. J., Grosse-Kunstleve, R. W., Storoni, L. C., and Read, R. J. (2005) *Acta Crystallogr. Sect. D Biol. Crystallogr.* **61,** 458–464
28. Grzesiek, S., and Bax, A. (1993) *J. Biomol. NMR* **3,** 185–204
29. Delaglio, F., Grzesiek, S., Vuister, G. W., Zhu, G., Pfeifer, J., and Bax, A. (1995) *J. Biomol. NMR* **6,** 277–293
30. Johnson, B. A., and Blevin, R. A. (1994) *J. Biomol. NMR* **4,** 603–614
31. Goddard, T. D., and Kneller, D. G. (1989) Sparky Version 3, University of California, San Francisco
32. Farrow, N. A., Zhang, O., Forman-Kay, J. D., and Kay, L. E. (1994) *J. Biomol. NMR* **4,** 727–734
33. Cheng, Y., Sequeira, S. M., Malinina, L., Tereshko, V., Sollner, T. H., and Patel, D. J. (2004) *Protein Sci.* **13,** 2665–2672
34. Ubach, J., Zhang, X., Shao, X., Sudhof, T. C., and Rizo, J. (1998) *EMBO J.* **17,** 3921–3930
35. Sutton, R. B., and Sprang, S. R. (1998) *Structure* (*Lond.*) **6,** 1395–1405
36. Ochoa, W. F., Corbalan-Garcia, S., Eritja, R., Rodriguez-Alfaro, J. A., Gomez-Fernandez, J. C., Fita, I., and Verdaguer, N. (2002) *J. Mol. Biol.* **320,** 277–291
37. Verdaguer, N., Corbalan-Garcia, S., Ochoa, W. F., Fita, I., and Gomez-Fernandez, J. C. (1999) *EMBO J.* **18,** 6329–6338
38. Malmberg, N. J., and Falke, J. J. (2005) *Annu. Rev. Biophys. Biomol. Struct.* **34,** 71–90
39. Fukuda, M., and Mikoshiba, K. (2000) *Biochem. Biophys. Res. Commun.* **276,** 626–632
40. Groffen, A. J., Friedrich, R., Brian, E. C., Ashery, U., and Verhage, M. (2006) *J. Neurochem.* **97,** 818–833
41. Sugita, S., Han, W., Butz, S., Liu, X., Fernandez-Chacon, R., Lao, Y., and Sudhof, T. C. (2001) *Neuron* **30,** 459–473
42. Scolastico, C., and Palazzi, C. M. F. G. (August 27, 1987) Italy, Patent WO 87/05024